White Rose Research Online

eprints@whiterose.ac.uk
https://eprints.whiterose.ac.uk
Universities of Leeds, Sheffield and York

Deposited via The University of Sheffield.

White Rose Research Online URL for this paper:
https://eprints.whiterose.ac.uk/id/eprint/129400/

Version: Accepted Version

Article:

Norris, D.J. and Walther, T. (2018) Stranski-Krastanow growth of (Si)Ge/Si(001): transmission electron microscopy compared with segregation theory. Materials Science and Technology, 34 (13). pp. 1539-1548. ISSN: 0267-0836

https://doi.org/10.1080/02670836.2018.1455013

Reuse

Items deposited in White Rose Research Online are protected by copyright, with all rights reserved unless indicated otherwise. They may be downloaded and/or printed for private study, or other acts as permitted by national copyright laws. The publisher or other rights holders may allow further reproduction and re-use of the full text version. This is indicated by the licence information on the White Rose Research Online record for the item.

Takedown

If you consider content in White Rose Research Online to be in breach of UK law, please notify us by emailing eprints@whiterose.ac.uk including the URL of the record and the reason for the withdrawal request.

UNIVERSITY OF LEEDS University of Sheffield UNIVERSITY of York

Note: Snapshot PDF is the proof copy of corrections marked in EditGenie, the layout would be different from typeset PDF and EditGenie editing view.

Author Queries:

Q1: The meaning of the sentence "Dividing the weighted Ge_K map…" is not clear. Please clarify.
Reply: The weighting is specified by the term following in brackets, hence should be clear from what has been explained before.

Comments:

Recto running head: MATERIALS SCIENCE AND TECHNOLOGY
Verso running head: D. NORRIS AND T. WALTHER
Copyright Line: © 2018 Institute of Materials, Minerals and Mining.

Stranski–Krastanov growth of (Si)Ge/Si(001): transmission electron microscopy compared with segregation theory

DJ Norris and T Walther

Department of Electronic and Electrical Engineering, University of Sheffield, Sheffield, UK

CONTACT T Walther t.walther@sheffield.ac.uk

History: received: 2018-01-19 revised: 2018-03-10 accepted: 2018-03-16

Abstract

We performed transmission electron microscopy of SiGe/Si(001) and Ge/Si(001) samples that undergo the Stranski–Krastanov transition from flat layer to island growth. With the help of quantitative X-ray maps of those layers, we have determined the total amount of deposited germanium at which islanding commences. The maximum amount of Ge buried in a flat layer amounts to 2.3 monolayers. We show by modelling that it is the strain due to the total amount of Ge atoms deposited that drives the islanding process. At 600°C [400°C], 1.62 [1.74] monolayers of Ge are expected from simulations to segregate towards the surface, the strain of which is sufficient to trigger plastic relaxation by islanding, in agreement with our electron microscope observations.

KEYWORDS: Stranski–Krastanov; islanding; SiGe; TEM; segregation; three-state exchange model

Introduction

The crystal growth of a strained alloy-based semiconducting heterostructure can proceed in one of two ways depending on the adatom content of the alloy concerned. By adatom, we mean foreign atoms deposited in an otherwise homoepitaxial layer, for example, Ge atoms in a (Si)Ge-on-Si heterostructure. Growth can proceed in a layer-by-layer fashion producing a relatively smooth surface morphology and this can remain flat to quite large thicknesses (>100 nm) prior to plastic relaxation via the nucleation of dislocation half loops (and associated stacking faults) from the surface. This is demonstrated in Figure 1(a) for a series of $Si_{0.77}Ge_{0.23}$/Si layers. Alternatively, the initial growth of heterolayers may proceed in a layer-by-layer manner for a few monolayers of growth whereupon the surface becomes unstable and atoms aggregate to form adatom rich islands. Such layer-by-layer growth (2D) followed by islanding (3D) is known as the Stranski–Krastanov transition. This phenomenon can be observed in a number of compressively strained heteroepitaxial systems such as SiGe/Si [1] and InGaAs/GaAs [2], where the latter produces quantum dots that can be used for light emitting device structures.

Figure 1. BF STEM images of samples #423 (a) and #424 (b), demonstrating the sharp onset of islanding at around x=0.28 Ge content. The arrow in (b) marks the first layer.

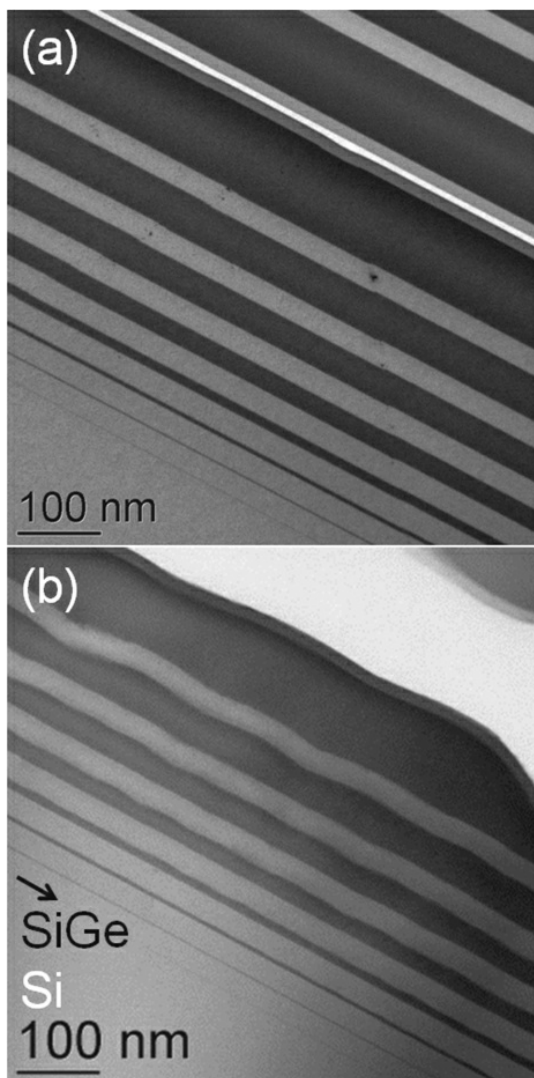

There is a specific, and abrupt, incident flux concentration (or chemical ratio) at which the Stranski–Krastanov transition from planar (2D) growth to islanding (3D) is triggered. For a $Si_{1-x}Ge_x$/Si epilayer, this critical concentration point is $x \approx 0.28$. For $x \leq 0.27$, layers are uniform and produce no islanding up to thicknesses in excess of 100 nm prior to plastic relaxation. For $x \geq 0.28$, islands tend to form after only a few monolayers of deposited material, see Figure 1(b) [3]. Pure Ge layers start to roughen earlier, after deposition of less than 3 monolayers on Si(001) [4], i.e. less than a full unit cell.

While there have been many studies of the Stranski–Krastanov transition in Ge or SiGe epitaxy over the last two decades, investigating the influence of the growth method used (mainly liquid phase epitaxy [5,6] vs. chemical vapour deposition [7-9] vs. molecular beam epitaxy [10-12]), the growth temperature [13,14,9,15], type of buffer layer [16], surface orientation (e.g. [14,17,18] for Si(111) instead of the more standard Si(001) orientation) or surface chemistry (C co-doping [19,20] and/or Sb surfactant treatment [21]), the phenomenon is sufficiently complex so a number of even basic questions have essentially remained open: it is, for example, still unclear whether for Ge on Si(111) the growth proceeds via a wetting layer [17,18] or not [22,23]. Also, the degree to which atomic interdiffusion [24-26], surface roughness [27,5] or an interplay of both effects [28] actually influence island nucleation is still a matter of debate. The central problem is related to actually detecting such a very thin wetting layer reliably and measuring its chemical composition [29,30].

In this report, we aim to elucidate reasons why such an abrupt transition from 2D to 3D growth should occur. In particular, we consider surface layer enrichment of larger adatoms (a consequence of segregation) as a likely explanation of the observed phenomenon. Experimental work by analytical transmission electron microscopy has been performed to deduce the critical thickness of layers prior to the nucleation of islands. This employed a novel method of extracting monolayer thicknesses from compositional maps derived from 2D X-ray mapping in the scanning transmission electron microscope (STEM), as described in [31,32], which has already been successfully applied to measure segregation to inversion domain boundaries [33] and to grain boundaries [34] to sub-monolayer accuracy. The measurements are compared to predictions made using a theoretical three-state atomic exchange segregation model [35] where intermixing of the top three monolayers deposited is considered instead of the conventional two-state models [36] the latter of which could not explain [37] the wide SiGe-on-Si interfaces observed experimentally [38].

Experimental details

$Si_{1-x}Ge_x$ and Ge layers were grown using reduced pressure chemical vapour deposition in an ASM Epsilon 2000 reactor, using germane and disilane gaseous precursors diluted in hydrogen as a carrier gas. The flow of precursor gases was adjusted independently to change the deposited alloy concentration. The growth details and specifications for these samples considered in this report are documented in Table 1.

Table 1. Growth parameters of the wafers investigated in this study.

Sample ID #	Growth temperature (°C)	(Si)Ge deposition time (s)	Nominal/ measured peak Ge content *x*
423	600	1, 2, 5, 10, 20, 30, 40, 80	0.27/0.23
424	600	1, 2, 5, 10, 20, 30, 40, 80	0.32/0.28
226	400	1*, 2, 3, 4, 5, 6	1/–
227	450	0.5, 1, 1.5, 2, 2.5, 3	1/–

*Layer not identified in Figure 3, hence possibly no effective deposition. The succeeding five layers have been identified and consecutively numbered according to their deposition times in seconds as #2–#6 in Figures 3–4.

---

[110] TEM specimens were made, in cross-section, by gluing pieces of material face to face and mechanically grinding and polishing each side to a final specimen thickness of 20–30 µm. Ceramic washers were glued with the region of interest centred and extraneous material surrounding the washer removed. After cleaning, specimens were argon ion beam thinned in a LEICA RES101 system at 5 kV and 2.5 mA to electron transparency followed by a low voltage (2 kV) polish to minimise amorphous material on the specimen surfaces.

Specimens were inserted into a JEOL 2010F field emission gun TEM operated at 197 keV and equipped with a liquid nitrogen cooled lithium drifted silicon (Si:Li) detector with ultrathin polymer window for X-ray spectrum analysis and imaging. Bright-field (BF) and annular dark-field (ADF) detectors were utilised throughout STEM operation. The X-ray detector is connected to hardware for energy pulse analysis through amplifiers and analog to digital conversion. Results are displayed on a PC containing a multichannel analyser via the Oxford Instrument ISIS300 X-ray analysis software from which spectroscopy and mapping are derived. The acquisition time for X-ray maps can be quite long (several hours) to get good Poisson statistics. During this acquisition, any drift that could be observed was corrected manually via the STEM x–y scan coils for each frame to an accuracy of 1–2 pixels (128 × 100 pixel image size, where 1 pixel = 1.15 nm at 800kX nominal magnification).

Determination of the effective chemical width of a layer

The objective of the present technique is to determine the Ge compositional profile in terms of concentration *x*(Ge) from the maps and deduce from this the chemical width of the (Si)Ge layer. Integration of the chemical profile provides the total Ge contained within the layer, giving an effective layer width corresponding to that of a pure Ge layer with the same number density of Ge atoms within it as the (Si)Ge layer.

The pertinent lines in the X-ray spectrum for mapping of (Si)Ge are the Si_K, Ge_K and Ge_L peaks. The X-ray maps in Figure 5 display the intensity of the energy ranges around these particular lines after an appropriate background subtraction made by linear interpolation.

The procedure for extracting the effective integrated layer width from the background subtracted Si_K, Ge_K and Ge_L maps is as described in [39] and briefly summarised here:

a. Define a box of 1 pixel height (*H*) of maximal length (*L*) extending to the edges of the layer of constant apparent width, as shown in Figure 5(g).
b. Take the integral of the counts of the map within this thin box of dimensions $H \times L$.
c. Increase the box height *H* by 1 pixel and repeat (b). The box should be increased in size symmetrically about the layer of interest so that the layer is centred within the box.
d. Do this until the box width has maximum height without impinging in proximity to other layers above, in our case 26 pixels or 30 nm high.
e. The procedure (a)–(d) should be done identically for each of the Si_K, Ge_K and Ge_L maps.
f. Calculate the Si_K/Ge_K and Si_K/Ge_L intensity ratios using Equation 1 and procedures outlined below.
g. Plot the Si_K/Ge_K and Si_K/Ge_L ratios as a function of box height *H*, as in Figure 6.
h. Perform a linear least squares fit of the data.
i. The inverse of the slope of the fit is the effective layer width where the Ge content condensed or contracted to produce a layer of pure Ge.

$$\frac{\mathrm{Si_K}}{\mathrm{Ge_{K,L}}} = \frac{I_{\mathrm{Si_K}}}{I_{\mathrm{Ge_{K,L}}}} \cdot \frac{k_{\mathrm{Si_K}}}{k_{\mathrm{Ge_{K,L}}}} \cdot \frac{\mathrm{abs}_{\mathrm{Si_K}}}{\mathrm{abs}_{\mathrm{Ge_{K,L}}}} \Big/ \frac{A_{\mathrm{Si}}}{A_{\mathrm{Ge}}} = \frac{I_{\mathrm{Si_K}}(H)}{I_{\mathrm{Ge_{K,L}}}(H)} \cdot \frac{1}{k^*_{\mathrm{Ge_{K,L}}}} \Big/ \frac{A_{\mathrm{Si}}}{A_{\mathrm{Ge}}}$$

where *I*(*H*) are the total counts of X-rays in the boxes of height *H* corresponding to the lines signified by the subscripts; *k* and abs are the *k*-factors with respect to weight percentages and absorption factors for the corresponding X-ray lines – these are both set to unity for Si as standard and accounted for together in an effective *k**-factor which was derived in previous work [40,41] and has previously been fitted for the K and L lines of Ge by the expressions in Equation (2) [42]. *A* denotes the relative atomic weight for Si and Ge, their ratio being $A_{Si}/A_{Ge} \approx 0.387$.

$$k^*_{\mathrm{Ge_K}} = 6.2639 \exp\left(-1.0971 \frac{I_{\mathrm{Ge_K}}}{I_{\mathrm{Ge_L}}}\right)$$
$$k^*_{\mathrm{Ge_L}} = 4.0617 \exp\left(-0.5389 \frac{I_{\mathrm{Ge_K}}}{I_{\mathrm{Ge_L}}}\right)$$

Results and discussion

Standard STEM imaging

BF STEM images of samples #423 (a) and #424 (b) are shown in Figure 1. As can be seen layers with Ge content of $x = 0.23$–0.27 stay flat up to well beyond 100 nm layer thicknesses, while occasional stacking faults bounded by partial dislocations can introduce nano-scale displacements of interfaces (a). If the Ge content is increased to $x = 0.28$–0.32, then only very thin SiGe layers remain flat (here: the first two) while thicker layers exhibit an increasing waviness (b). The concentration ranges given refer to the Ge content measured by quantitative EDXS (lower values) and the nominal values (upper values). In [3], the Stranski–Krastanov transition related to this sudden onset of roughening has been determined to lie around $x = 0.28 \pm 0.01$ for $Si_{1-x}Ge_x$ layers grown at 600°C. The first layer deposited of sample #424 and indicated by an arrow in Figure 1(b) is only faintly visible in BF but invisible in annular dark-field (ADF) conditions which is why the third layer imaged by high-resolution electron microscopy (HREM) in Figure 2 was erroneously reported as second layer in [39]. This layer shows a perfect crystal lattice but clearly a slightly diffuse and wavy upper interface.

Figure 2. HREM image of the third layer from sample #424, revealing a ~1.6 nm thin SiGe layer which already shows some very slight lateral thickness variations.

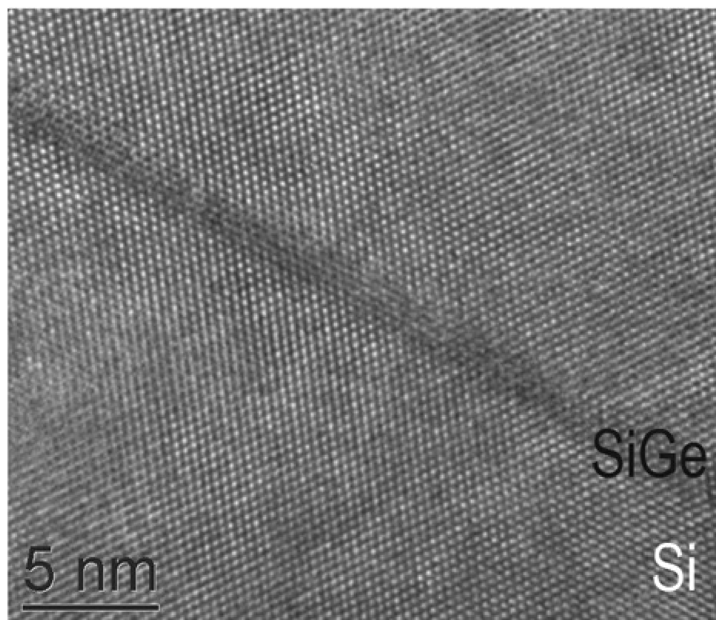

A BF STEM image (Figure 3) obtained from sample #226 shows a series of thin layers rich in Ge (nominally pure Ge). In this image five layers are visible, albeit the lowest only very weakly; comparing this to the deposition sequence indicates that for the first second, no deposition has taken place. Layers #2−#4 marked by arrows in Figure 3 appear uniformly flat, but as the deposition time increases, and with this the thickness of the Ge layer, we find that Ge-rich islands form and grow from layer #5 onwards. Figure 4 shows, again, that the last flat layer (#4) is ~1.5 nm thin and reveals perfect epitaxy and flat interfaces (b) while the first wavy Ge layer (#5) already introduces islands and lattice defects (a) that then propagate through the crystalline Si cap layer.

Figure 3. BF STEM image of samples #226, demonstrating the sharp onset of islanding for nominally pure Ge deposition. For the first second, there did not appear to be any deposition taking place at 400°C, as only five instead of six layers are visible. These are labelled according to their deposition time in seconds as #2−#6. The arrows mark flat layers #2−#4.

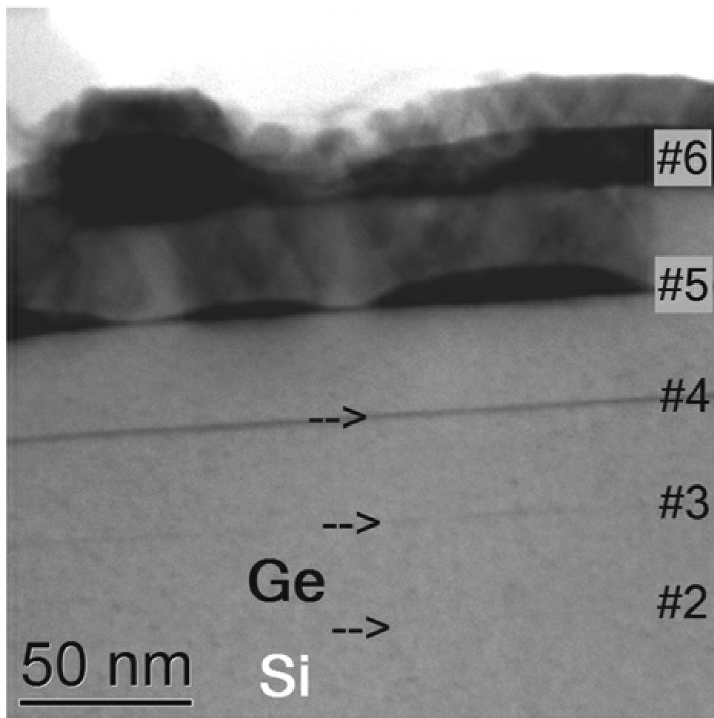

Figure 4. HREM images from sample #226 of (a) first islanded layer #5 and (b) uppermost flat layer #4 (marked by top arrow in Figure 3).

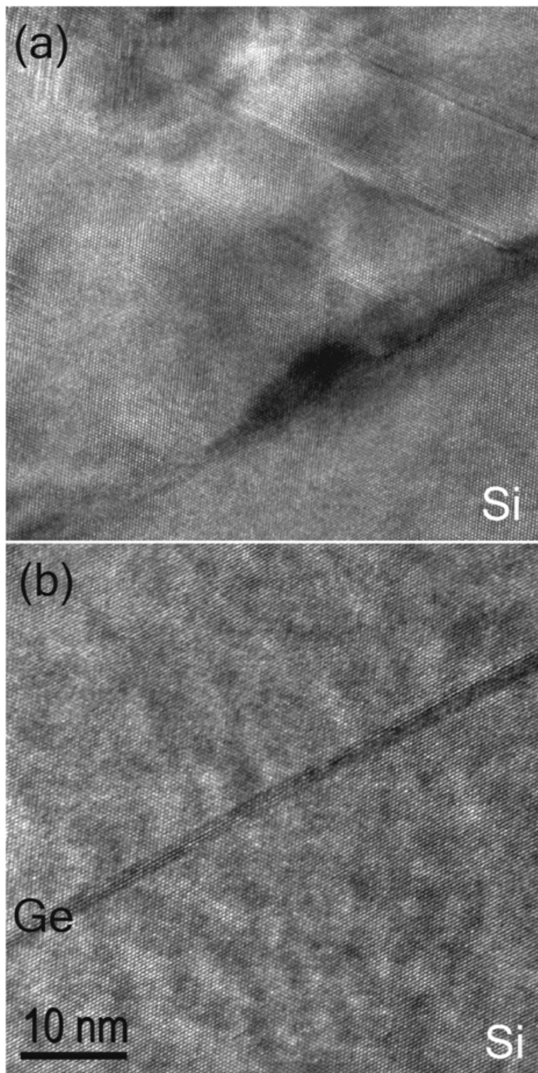

Sample #227 grown at a temperature elevated by only 50°C relative to #226 showed a very similar structure, and in the

following we concentrate on this sample.

Determination of Ge concentration maps

Various X-ray maps (a–c) and processed maps (d–g) for sample #227 are shown in Figure 5: the upper row shows maps acquired with windows ~~painted in~~integrating the X-ray spectrum for (a) the Si_K, (b) Ge_L and (c) Ge_K edges with appropriate background subtraction applied. The objective is to determine Ge concentration maps and from these the effective amounts of Ge incorporated in the topmost flat and the first islanded layer, which requires a number of steps as described by the lower maps (d–g). We need to deduce an effective k^*-factor for each pixel in the relevant X-ray map for which the fit from Equation (2) shows that we need the $Ge_{K/L}$ ratio depicted in Figure 5(d). The resulting $k^*_{Ge\text{-}K}$ map from Equation (2) is shown in Figure 5(e). The next step is to calculate the sum of Si_K+Ge_K, however, the Ge-K map should be weighted (multiplied) with the appropriate $k^*_{Ge\text{-}K}$ factor and multiplied by the ratio of the (Si/Ge) atomic weights given in Equation (1); this is shown in Figure 5(f). This weighted Si_K+Ge_K map should be mainly featureless (as observed) and only contains contrast due to specimen thickness variations and selective surface oxidation.

Figure 5. X-ray analysis of sample #227. Top row: X-ray maps of the lines of Si K (a, max = 45), Ge L (b, max = 23) and Ge K (c, max = 25). Middle row: Processed maps of Ge K/L ratio (d, range 0–3), corresponding *k factor of the Ge K line (e , range 0–6) and the sum of Si and Ge signals with the later weighted by *k** and ratio of atomic weights (which should ideally show only thickness dependence but no layer features); bottom row: map of *x*(Ge) = (c)/(f) in pseudo-colour (g, range: 0–1.3) with boxes for calculation of the signals and horizontally integrated profile of *x*(Ge) showing Ge content in the layers (h).**

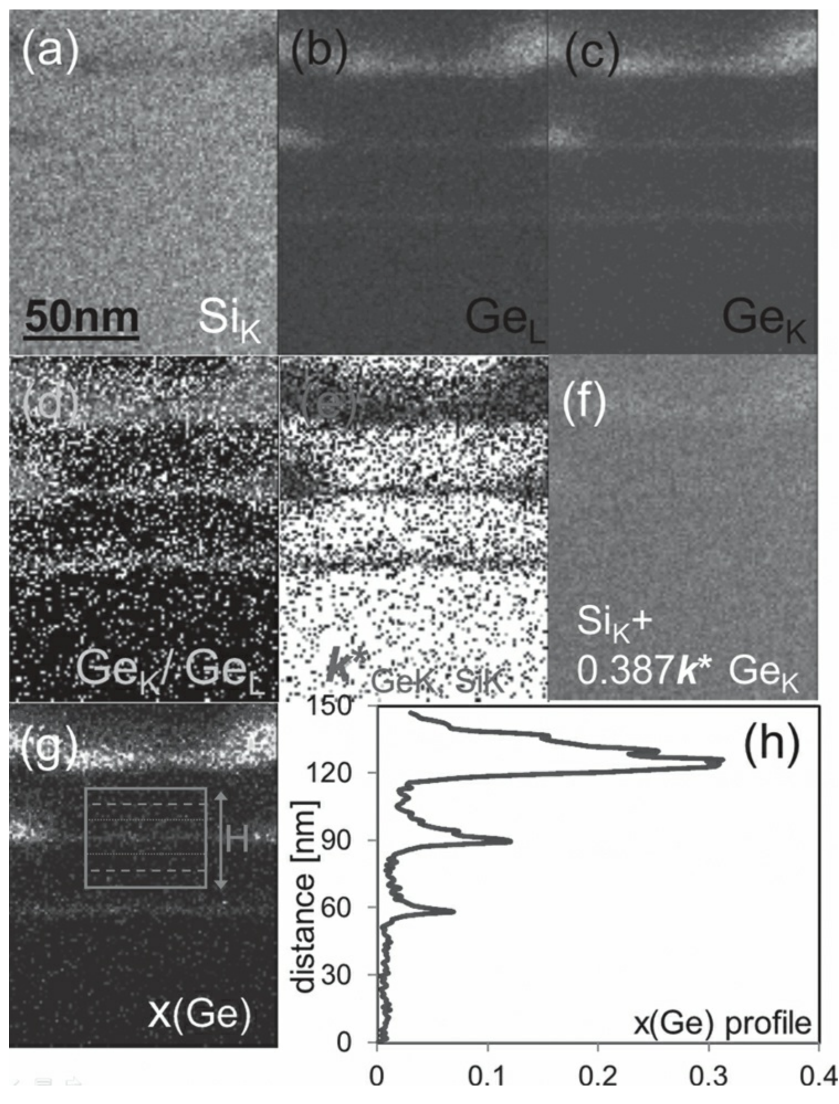

Dividing the weighted[Q1] Ge_K map (i.e. again multiplied by the effective k^*-factor and the ratio of the atomic weights) divided by the above weighted sum I_{SiK}+0.387 k^*_{GeK} I_{GeK} gives the final Ge concentration map from K lines, shown in Figure 5(g) along with a an integrated profile line scan in Figure 5(h). Corresponding processing of the Ge_L map yields an x(Ge) map from using this line, and both maps agree to within noise levels.

Determination of effective Ge layer thicknesses using window method

The procedure outlined in Section 3 was applied to the maps in Figure 5, where the topmost uniformly flat layer has been considered in Figure 6(b) and the flat region between islands (i.e. the wetting layer after islanding as outlined in Figure 5(g))

was analysed in Figure 6(a). The results, reproduced from [39], are for Ge K- and L-lines with k^* factors from either the individual maps or for a noise averaged Ge K/L ratio of 1.4. The inverse of the slopes of the lines fitted to these data using linear least squares methods is a direct measure of the effective total amount of Ge within these thin layers [31,32] and results are listed in Table 2 in multiples of equivalent full monolayers of Ge (where 1 ML = $a/4$ = 0.136 nm for (001)Si). This provides a lower estimate of 2.05 ± 0.06 ML for the Ge content in the uppermost flat layer and an upper estimate of 2.76 ± 0.22 ML for the Ge content in the flat part of the first islanding layer. Somewhere in-between, at around 2.4 ML, the Stranski–Krastanov transition must take place. Similar values have been found for the $Si_{0.72}Ge_{0.28}$ sample #424 and the Ge sample #226 [39]. This, however, is only the amount of Ge in the thin (Si)Ge layers; there is an additional amount of Ge accumulating on the wafer surface during growth, which low energy electron diffraction (LEED) estimated as 0.9 ML [43], reflection high-energy electron diffraction (RHEED) as 0.75 ML [44], Auger spectroscopy as 0.8 ML [45] and STEM-EELS as 0.6 ML [46]. This Ge-rich surface monolayer also exists for Ge deposition on differently oriented Si substrates [23].

Figure 6. Plots of Si/Ge ratios as function of height of integration window for flat region of first islanded layer (a) and uppermost flat layer (b) from sample #227.

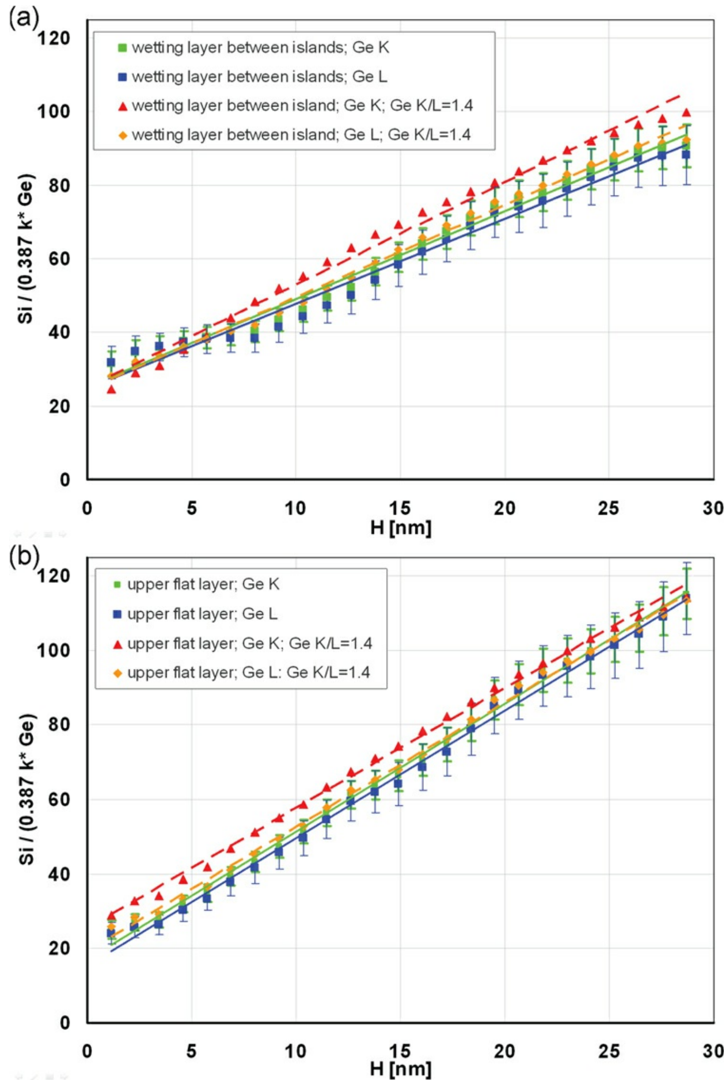

Table 2. Numerical analysis of layers of wafer #227 by analytical STEM (Figures 5–6).

Method	Line	Total Ge deposited in layer [ML]	Error bar [ML]	Remark for SK onset
Slope of Si/Ge ratio vs. H from map for variable Ge K/L intensity	K	Between islands: 2.87	±0.07	R^2 = 0.9858
		Upper flat: 2.00	±0.02	R^2 = 0.9965
	L	Between islands: 2.98	±0.09	R^2 = 0.9786
		Upper flat: 2.01	±0.03	R^2 = 0.9957
Slope of Si/Ge ratio vs. H for Ge K/L intensity = 1.4	K	Between islands: 2.46	±0.05	R^2 = 0.9891
		Upper flat: 2.13	±0.02	R^2 = 0.9970

Method	Line	Total Ge deposited in layer [ML]	Error bar [ML]	Remark for SK onset
	L	Between islands: 2.74	±0.04	$R^2 = 0.9943$
		Upper flat: 2.06	±0.02	$R^2 = 0.9974$
Average	All	2.41	±0.41	
Upper estimate for wetting layer between islands	All	2.76	±0.22	
Lower estimate from top flat layer	All	2.05	±0.06	
Simulation	–	2.29	–	+0.71 ML just under surface

Segregation modelling

Figure 7 sketches the result from applying the segregation model with atomic exchanges between the top three monolayers, called the three-state exchange model [35], for a perfectly flat (001) specimen surface with an activation energy for surface segregation of 1.40 eV and segregation energies of 0.13 eV, which are both significantly lower than corresponding values from the original two-state exchange model [36]. Interestingly, it was found by pseudopotential modelling [47] that if there is sufficient Ge coverage, Ge dimers form on the Si(001) surface that are tilted, and the difference between the up-atom and down-atom configurations has also been found to be 0.13 eV, so may be directly related to the segregation energy. The effect of surface segregation is that for the leading (Si)Ge-on-Si interface the deposited Ge amount lags behind the deposition flux for several monolayers, the Ge difference being stored in the topmost (two-state exchange model) or the two topmost (three-state exchange model) monolayer(s) which therefore become significantly enriched. When the supplied flux stops, the trailing Si-on-(Si)Ge interface exhibits an exponential tail (and is shifted inwards by one to two monolayers as can be seen in simulations such as Figure 7) as the Ge enrichment from the surface is gradually incorporated during Si overgrowth, leaving behind only slightly Ge-enriched surface monolayer(s). It is the persistence of the latter during overgrowth by Si that has been detected by surface analysis techniques and led to many segregation studies in the first place.

Figure 7. Sketch of Ge surface segregation modelled. Only a fraction of incoming Ge flux (green: $x_{nom} = 0.25$) is incorporated into the SiGe layer (blue) while a high fraction segregates to the top monolayer surface (red) and the monolayer directly underneath (not shown here) where it accumulates until the deposition flux is switched off.

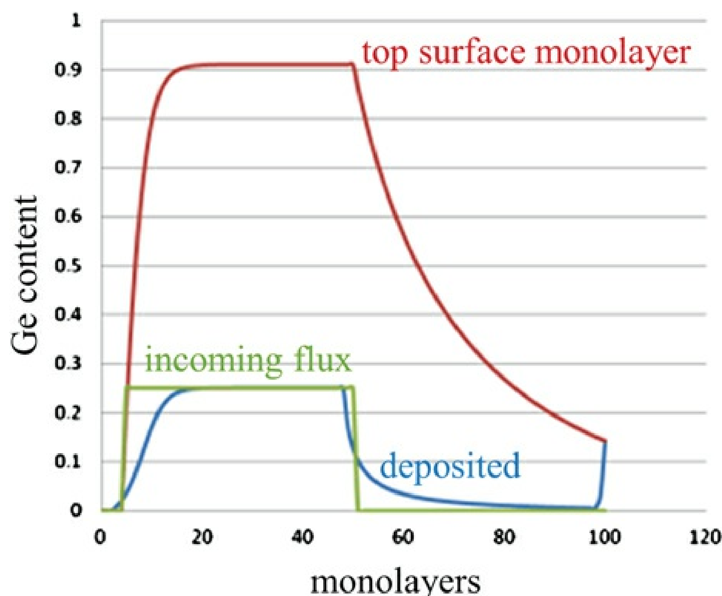

In Figures 8 and 9, we plot the sum of the Ge content within the two topmost monolayers calculated using the three-state exchange model for various deposition fluxes and two different growth temperatures. It is conspicuous that for fluxes of $x \geq 0.28$, for which the Stranski–Krastanov transition is experimentally observed, this total Ge excess on the surface reaches values of ~1.7 monolayers (1.74 ML at 400°C in Figure 8, 1.62 ML at 600°C in Figure 9) after deposition of 2.3–2.5 ML pure Ge or 12 ML $Si_{0.72}Ge_{0.28}$, which corresponds well to the integrated Ge amount we measured using STEM-EDXS in our SiGe layers. From this we conclude that it is the total strain energy contained within ~1.7 ML of Ge on the surface by the segregation mechanism which is responsible for the sudden transition from flat layer to island growth observed. For a deposition flux $x < 0.28$, this surface enrichment will never build up and arbitrarily thick layers of $Si_{1-x}Ge_x$ can be grown that remain flat, as demonstrated in Figure 1(a). For a flux of $x = 0.28$, up to nominally about 12 ML can be deposited for the film to remain flat; at this point the film will contain ~(12*0.28–1) ML = 2.36 ML Ge (the 1 ML having accumulated at the surface). For pure Ge deposition, ~3 ML can be deposited of which the film will retain 2.3 ML and 0.7 ML will accumulate on the surface.

Figure 8. Ge segregation model for different deposition fluxes at 400°C.

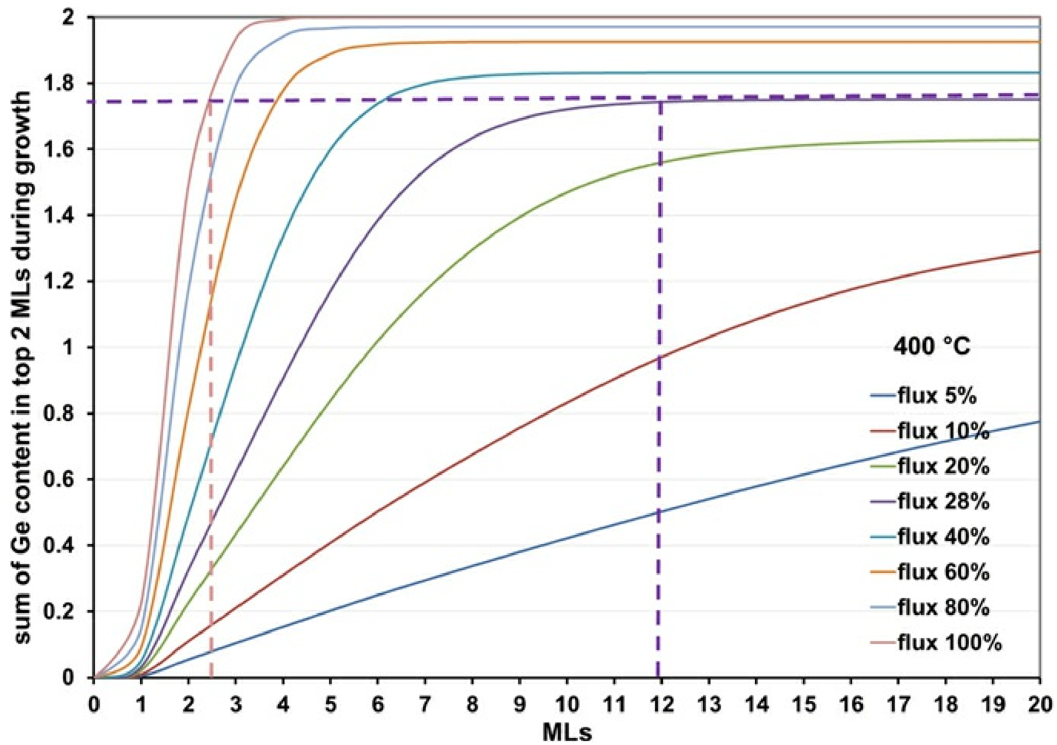

Figure 9. Ge segregation model for different deposition fluxes at 600°C.

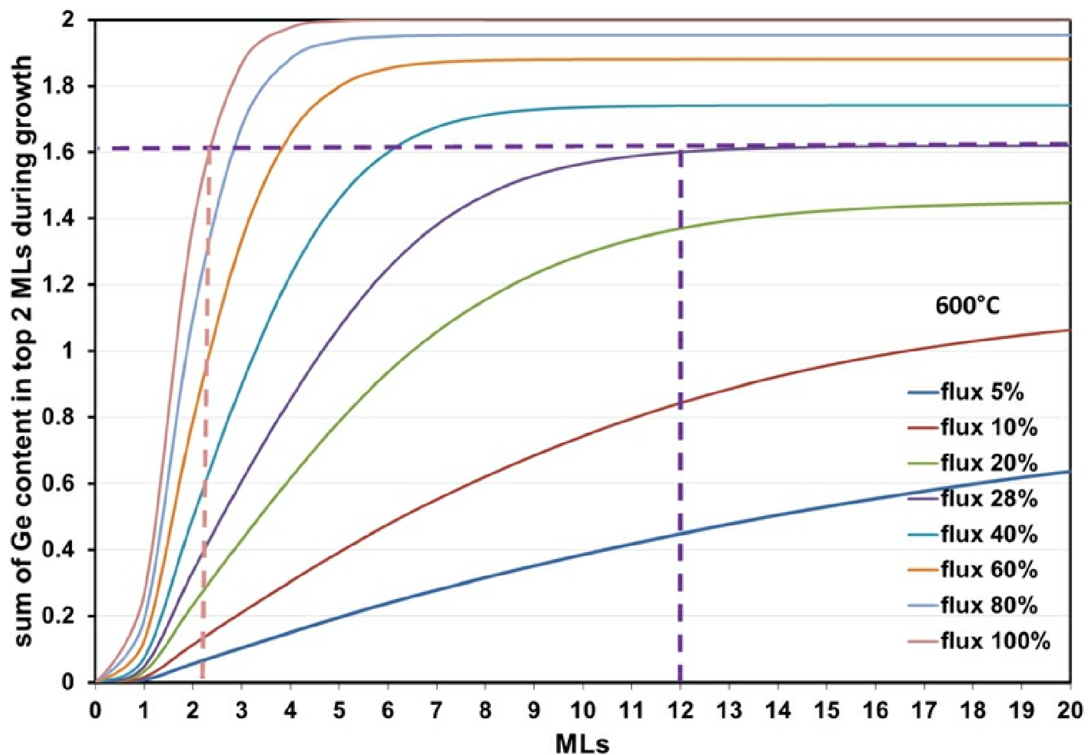

Conclusion

We have measured the total Ge content in thin layers of SiGe and Ge deposited on Si(001) and compared the results to simulations using a three-state exchange model for Ge surface segregation. The good agreement explains why $Si_{1-x}Ge_x$ films for $x < 0.28$ can remain flat while for $x \geq 0.28$ the Stranski–Krastanov growth is observed instead.

Funding

This work was supported by Engineering and Physical Sciences Research Council: [Grant Number EP/F033893/1].

Acknowledgement

The authors thank the Engineering and Physical Sciences Research Council for financial support of this work under grant number EP/F033893/1 'Renaissance Germanium'.

Disclosure statement

No potential conflict of interest was reported by the authors.

References

1 Eaglesham DJ, Cerullo M. Dislocation-free Stranski–Krastanov growth of Ge on Si(100). Phys Rev Lett. 1990;64(16):1943–1946.

2 Cullis AG, Norris DJ, Walther T, et al. Stranski–Krastanov transition and epitaxial island growth. Phys Rev B. 2002;66:81305R.1–4.

3 Walther T, Norris DJ, Qiu Y, et al. The Stranski–Krastanov transition in SiGe epitaxy investigated by scanning transmission electron microscopy. Phys Stat Sol (a). 2013;210(1):187–190.

4 Mo Y-W, Savage DE, Swartzentruber BS, et al. Kinetic pathway in Stranski–Krastanov growth of Ge on Si(001). Phys Rev Lett. 1990;65(8):1020–1023.

5 Hanke M, Schmidbauer M, Grigoriev D, et al. SiGe/Si(001) Stranski–Krastanov islands by liquid-phase epitaxy: diffuse X-ray scattering versus growth observations. Phys Rev B. 2004;69(7):3691.

6 Schade M, Heyroth F, Syrowatka F, et al. Investigation of the chemical composition profile of SiGe/Si(001) islands by analytical transmission electron microscopy. Appl Phys Lett. 2007;90(26):263101.

7 Ross FM, Tersoff J, Tromp RM. Ostwald ripening of self-assembled germanium islands on Silicon(100). Microsc Microanal. 1998;4(3):254–263.

8 Le Thanh V. New insight into the kinetics of Stranski–Krastanov growth of Ge on Si(001). Surf Sci. 2001;492(3):255–269.

9 Halbwax M, Bouchier D, Yam V, et al. Kinetics of Ge growth at low temperature on Si(001) by ultrahigh vacuum chemical vapor deposition. J Appl Phys. 2005;97(6):064907.

10 Pinto N, Murri R, Trojani L, et al. Advances in crystal growth. Mater Sci Forum. 1996;203:79–84.

11 Jiang WR, Qin J, Hu DZ, et al. A two-stage molecular beam epitaxial growth method to fabricate small and uniform Ge quantum dots on Si(100). J Cryst Growth. 2001;227–228:1106–1110.

12 Volpi F, Peaker AR, Hawkins ID, et al. Hole trapping in self-assembled SiGe quantum nanostructures. Mater Sci Eng B. 2003;101(1–3):338–344.

13 Hammer M, LeGoues FK, Tersoff J, et al. In situ ultrahigh vacuum transmission electron microscopy studies of hetero-epitaxial growth. 1. Si(001)/Ge. Surf Sci. 1996;349(2):129–144.

14 Walz J, Greuer A, Wedler G, et al. Stress and relief of misfit strain of Ge/Si(111). Appl Phys Lett. 1998;73(18):2579–2581.

15 Grimm A, Fissel A, Bugiel E, et al. In situ observation of low temperature growth of Ge on Si(111) by reflection high energy electron diffraction. Appl Surf Sci. 2016;370:40–48.

16 Zhang ZP, Song YX, Chen QM, et al. Growth mode of tensile-strained Ge quantum dots grown by molecular beam epitaxy. J Phys D Appl Phys. 2017;50(46):465301.

17 Shklyaev AA, Shibata M, Ichikawa M. Instability of two-dimensional layers in the Stranski–Krastanov growth mode of Ge on Si(111). Phys Rev B. 1998;58(23):15647–15651.

18 Shklyaev AA, Shibata M, Ichikawa M. Instability of 2D Ge layer near the transition to 3D islands on Si(111). Thin Solid Films. 1999;343–344:532–536.

19 Leifel O, Beyer A, Müller E, et al. Formation and ordering effects of C-induced Ge dots grown on Si (001) by molecular beam epitaxy. Mater Sci Eng B. 2000;74(1–3):222–228.

20 Dentel D, Bischoff JL, Kubler L, et al. Influence of a pre-deposited carbon submonolayer on the Ge island nucleation on Si(001). J Appl Phys. 2003;93(9):5069–5074.

21 Osten HJ, Bugiel E, Zaumseil P. Antimony-mediated growth of epitaxial $Ge_{1-Y}C_Y$ layers on Si(001). J Cryst Growth. 1994;142(3–4):322–326.

22 Albrecht M, Hansson PO, Christiansen S, et al. Balancing surface-energy terms for stable growth of planar surfaces. Scan Microsc. 1994;8(4):925–934.

23 Norris DJ, Myronov M, Leadley DR, et al. Comparison of cross-sectional transmission electron microscope studies of thin germanium epilayers grown on differently oriented silicon wafers. J Microsc. 2017;268(3):288–297.

24 Ide T, Sakai A, Shimizu K. Nanometer-scale imaging of strain in Ge islands on Si(001) surface. Thin Solid Films. 1999;357(1):22–25.

25 Portavoce A, Hoummada K, Ronda A, et al. Si/Ge intermixing during Ge Stranski–Krastanov growth. Beilstein J Nanotechnol. 2014;5:2374–2382.

26 Brehm M, Groiss H, Bauer G, et al. Atomic structure and composition distribution in wetting layers and islands of germanium grown on Silicon (001) substrates. Nanotechnol. 2015;26(48):485702.

27 Thanh V L, Yam V. Superlattices of self-assembled Ge/Si(001) quantum dots. Appl Surf Sci. 2003;212–213:296–304.

28 Walther T, Humphreys CJ, Cullis AG, et al. A correlation between compositional fluctuations and surface undulations in strained layer epitaxy. Mater Sci Forum. 1995;196–201:505–510.

29 Walther T. Determining buried wetting layer thicknesses to sub-monolayer precision by linear regression analysis of series of spectra. Proc. MSM-15, Cambridge. Springer Proc Phys. 2007;12:247–250.

30 Walther T. A comparison of transmission electron microscopy methods to measure wetting layer thicknesses to sub-monolayer precision. Proc. EMAG2007, Glasgow. J Phys Conf Ser. 2008;126:012091.

31 Walther T. Development of a new analytical electron microscopy technique to quantify the chemistry of planar defects and to measure accurately solute segregation to grain boundaries. J Microsc. 2004;215:191–202.

32 Walther T. Linear least-squares fit evaluation of series of analytical spectra from planar defects: extension and possible implementations in scanning transmission electron microscopy. J Microsc. 2006;223:165–170.

33 Walther T, Recnik A, Daneu N. A novel method of analytical transmission electron microscopy for measuring highly accurately segregation to special grain boundaries and planar defects. Microchim Acta. 2006;155:313–318.

34 Walther T. Accurate measurement of atomic segregation to grain boundaries or to planar faults by analytical transmission electron microscopy. Phys Stat Sol (c). 2015;12:310–313.

35 Godbey DJ, Ancona MG. Modelling of Ge segregation in the limits of zero and infinite surface diffusion. J Vac Sci Technol A. 1997;15(3):976–980.

36 Fukatsu S, Fujita K, Yaguchi H, et al. Self-limitation in the surface segregation of Ge atoms during Si molecular-beam epitaxial growth. Appl Phys Lett. 1991;59(17):2103–2105.

37 Godbey DJ, Ancona MG. Analysis of Ge segregation in Si using a simultaneous growth and exchange model. Surf Sci. 1998;395(1):60–68.

38 Walther T, Humphreys CJ, Robbins DJ. Diffusion and surface segregation in thin SiGe/Si layers studied by scanning transmission electron microscopy. Defect Diffusion Forum. 1997;143–147(2):1135–1140.

39 Norris DJ, Qiu Y, Dobbie A, et al. Similarity of Stranski–Krastanov growth of Ge/Si and SiGe/Si. J Appl Phys. 2014;115(1):012003.

40 Walther T. An improved approach to quantitative X-ray microanalysis in (S)TEM: thickness dependent k-factors. Proc. EMAG2009, Sheffield. J Phys Conf Ser. 2010;241:012016.

41 Walther T, Wang X. Self-consistent absorption correction for quantitative energy-dispersive X-ray spectroscopy of InGaN layers in analytical transmission electron microscopy. Proc. EMAG 2015, Manchester. J Phys Conf Ser. 2015;644:012006.

42 Qiu Y, Nguyen VH, Dobbie A, et al. Calibration of thickness-dependent *k*-factors for germanium X-ray lines to improve energy-dispersive X-ray spectroscopy of SiGe layers in analytical transmission electron microscopy. Proc. MSM-18, Oxford. J Phys Conf Ser. 2013;471:012031.

43 Butz R, Kampers S. 2×*n* surface structure of SiGe layers deposited on Si(100). Appl Phys Lett. 1992;61(11):1307–1309.

44 Li Y, Hembree GG, Venables JA. Quantitative Auger electron spectroscopic analysis of Ge surface segregation in Si/Ge/Si(100) heterostructures. Appl Phys Lett. 1995;67(2):276–278.

45 Nyéki J, Girardeaux Ch, Erdélyi Z, et al. AES study of surface segregation of Ge in amorphous $Si_{1-x}Ge_x$ thin film alloys. Surf Sci. 2001;495:195–203.

46 Walther T, Humphreys CJ, Cullis AG. Observation of vertical and lateral Ge segregation in thin undulating SiGe layers on Si by electron energy loss spectroscopy. Appl Phys Lett. 1997;71(6):809–811.

47 Cho J-H, Jeong S, Kang M-H. Final-state pseudopotential theory for the Ge 3*d* core-level shifts on the Ge/Si(100)-(2 × 1) surface. Phys Rev B. 1994;50(23):17139–17142.